

## 4D printed orbital stent for the treatment of enophthalmic invagination

Yongdie Deng<sup>a,1</sup>, Binbin Yang<sup>b,1</sup>, Fenghua Zhang<sup>a</sup>, Yanju Liu<sup>c</sup>, Jingbo Sun<sup>b</sup>, Shiqi Zhang<sup>b</sup>, Yutong Zhao<sup>b</sup>, Huiping Yuan<sup>b,\*\*</sup>, Jinsong Leng<sup>a,\*</sup>

<sup>a</sup> Centre for Composite Materials and Structures, Harbin Institute of Technology, No.2 Yikuang Street, Harbin, 150080, People's Republic of China

<sup>b</sup> Department of Ophthalmology, The 2nd Affiliated Hospital of Harbin Medical University, No. 246 Xuefu Road, Harbin, 150001, People's Republic of China

<sup>c</sup> Department of Astronautical Science and Mechanics, Harbin Institute of Technology, No. 92 West Dazhi Street, Harbin, 150001, People's Republic of China

### ARTICLE INFO

#### Keywords:

Shape memory polyurethane  
Enophthalmos  
4D printing  
CT development  
Volume filling  
Bionic design

### ABSTRACT

Currently, the implants used for enophthalmic invagination have the disadvantages of precise filling difficulty, weak filling ability, large surgical wounds, and lack of CT development. Here, a CT-developable orbital stent was manufactured via 4D printing of a shape memory polyurethane composite for enophthalmos treatment. The composite was endowed with good CT development properties via incorporation of gold nanoparticles and nano-hydroxyapatite. Based on the bionic idea and CT reconstruction technique, a 4D printed orbital stent with a bionic honeycomb pore structure and an outer contour matching the orbital coloboma was designed to support the orbital tissue more accurately and stably. CT images of rabbits before and after the 4D printed orbital stent implantation showed better volume-filling capacity compared with the two types of the commercial orbital implants. The three-month follow-up showed the good postoperative result, which demonstrated the excellent performance of the composite in the precise minimally invasive treatment of enophthalmos compared with traditional orbital implants.

### 1. Introduction

Shape memory polymers (SMPs), as a series of stimuli-responsive smart materials, can realize conversion between temporary and permanent shapes under external stimulation, including heat [1–4], electric fields [5], light [6,7], magnetic fields [8,9], and solutions [10]. Heat-driven SMPs, which achieve shape recovery by directly heating above their transition temperatures ( $T_{trans}$ ), have been widely investigated. Among them, shape memory polyurethane (SMPU), with a molecular microphase structure, has a  $T_{trans}$  determined by the melting point of the soft segment and a permanent shape determined by the hard segment [11]. Polyester SMPU, an important hydrolytically and enzymatically degradable polymer, has adjustable  $T_{trans}$ , good mechanical properties, good antithrombogenicity, and biocompatibility, making it a promising implantable material in the biomedical field [12]. Through 4D printing technology, the SMPs would have more application opportunities, such as intelligent structures. As one of the most advanced manufacturing techniques, 4D printing can manufacture structures with complexity and fineness, and also allows structures to be programmed to

change configurations, features, and functions on demand [13]. 4D printing SMPs have unique advantages and have been actively researched in the field of biomedical structures because of their ability to manufacture personalized medical structures and the possibility of dynamic and controllable structural transformation to meet different needs [14–16]. It is of great significance to achieve minimally invasive surgery (MIS) and personalized treatment in clinical biomedical applications, such as enophthalmos.

Enophthalmos refers to a phenomenon in which a normal-sized globe shows relative posterior displacement in relation to the bony orbital margin, which is usually secondary to nontraumatic or orbital trauma [17,18]. One of the primary objectives of correcting enophthalmos is to fill the orbital volume to restore facial appearance by implanting [19, 20]. However, implants used to treat enophthalmos have some difficulties to overcome. First, it is difficult to accurately match the contour of orbital coloboma using commonly used clinical implants. Second, the development of implants on CT directly affects the evaluation of postoperative surgical results. Based on the CT technique, clinical enophthalmos can be evaluated using orbital volume measurements (OVMS)

\* Corresponding author..

\*\* Corresponding author. .

E-mail addresses: [yuanhp2013@126.com](mailto:yuanhp2013@126.com) (H. Yuan), [lengjs@hit.edu.cn](mailto:lengjs@hit.edu.cn) (J. Leng).

<sup>1</sup> These authors contributed equally to this work.

[21,22]. Implants without CT development, such as Medpor and absorbable plates, are difficult to evaluate clinically [23]. Third, many implants do not have sufficient volumetric filling capacity to achieve good facial recovery [24]. In addition, larger surgical wounds are always clinically required to implant an implant that can fully fill the orbital coloboma, bringing more harm to patients. To overcome these difficulties, it is necessary to develop a customizable orbital implant with radiographic development and a smart compressible-deployable structure. Fortunately, 4D printing of SMPU-based composites provides an appropriate approach for overcoming the difficulties in treating enophthalmos.

Herein, a AuNPs/nHA/SMPU (AHP) composite with excellent CT developability was prepared by incorporating gold nanoparticles (AuNPs) and nano-hydroxyapatite (nHA) into SMPU. Based on the composite, a 4D printed orbital stent with X-ray development and shape memory property was manufactured by a 3D-Bioplotter in a convenient, clean and safe way to treat enophthalmos. The orbital stent was designed by combining the bionics design and CT reconstruction technology. The volume filling capacity of the stent was compared with two kinds of commercial implants including Medpor and absorbable plates. Then, the three-month follow-up was performed to research the post-operative result of the AHP stent. Combining CT-developable SMP composites and 4D printing, the urgent demands of MIS, observable evaluation and personalized treatment of enophthalmos can be met.

## 2. Results and discussion

### 2.1. Characterization on the AHP composite

The sagittal plane of the eye shows (Fig. 1A), the eyeball located in the orbital wall, surrounded by the muscles, soft tissue and fat around eyeball. As shown in Fig. 1B, the normal-sized globe appears as a relative posterior displacement to the bony orbital margin following orbital wall fractures. Here, an orbital stent, prepared with the AHP composite, was compressed to a flat temporary shape and subsequently implanted into the orbit, which can recover its permanent shape under thermal stimulus to fill the orbital coloboma and restore the volume, making the eyeball normal. The AHP composite was prepared by adding nHA suspension liquid and AuNP colloid to the SMPU emulsion (PU) (Fig. 1C). nHA can improve the protein and osteoblast adsorption performance of the PU matrix and its mechanical properties [25]. The addition of AuNPs can

result in higher contrast under X-ray radiation [26]. AuNPs possess favorable X-ray attenuating properties and provide approximately 2.7 times greater contrast per unit weight than iodine [27]. In addition, AuNPs can effectively prolong residence time in blood circulation and reduce toxicity to the kidneys [28]. To explore the effect of adding AuNPs and nHA, AHP film with 0.2 wt% AuNPs and 10 wt% nHA, nHA/PU (HP) film with 10 wt% nHA and AuNPs/PU (AP) film with 0.2 wt% AuNPs were prepared by drying AHP, HP and AP mixtures, respectively.

Microscopic images of the AHP mixture (Supp. Fig. S1) and UV-vis absorption spectra, showing obvious absorption peaks at 520.3 nm (Supp. Fig. S2) indicated that AuNPs and nHA did not agglomerate during the mixing process of AHP mixture preparation. The addition of HP and AuNPs did not alter the chemical bonds of the matrix (Supp. Fig. S3); however it can improve the thermal stability (Supp. Fig. S4). As shown in Fig. 1D, the  $T_{\text{trans}}$  of AHP is 42.5 °C, which is close to body temperature. At 44 °C, the AHP film recovered from a temporary to a permanent shape within 8 s. Following five shape-memory cycles, the recovery rate (Rr) and fixed rate (Rf) of AHP films with a thickness of 0.4 mm were still above 95% and 93%, respectively, which indicates that the AHP composite has good shape memory performance (Supp. Fig. S5). A preliminary study on the X-ray development of AHP, AP, HP, and PU films with a thickness of 0.5 mm and iodohyalcohol (IC) developer (0.2 wt%, Shanghai Aladdin Biochemical Technology Co., Ltd, China) with a liquid height of 0.5 mm was conducted using CT scanning (Fig. 1E). It can be seen that the gray values of the AP and AHP composite with 0.2 wt% AuNPs increased by nearly 100% compared with the iodine developer and nearly 120% compared with PU, which preliminarily verifies that the AHP composite meets visibility requirements. Hence, the AHP composite is a suitable implant material for manufacturing orbital stents to treat enophthalmos with observable monitoring.

### 2.2. Bionic pore structure

A qualified orbital stent for treating enophthalmos needs to meet two requirements: the pore structure required for cell growth and nutrient transport, and the mechanical strength needed for cell growth [29,30]. Pore geometry, pore size, and porosity can affect the transportability and mechanical properties of stents [31,32]. The orbital stent is subjected to pressure and tension from the adjacent tissues. For a specific

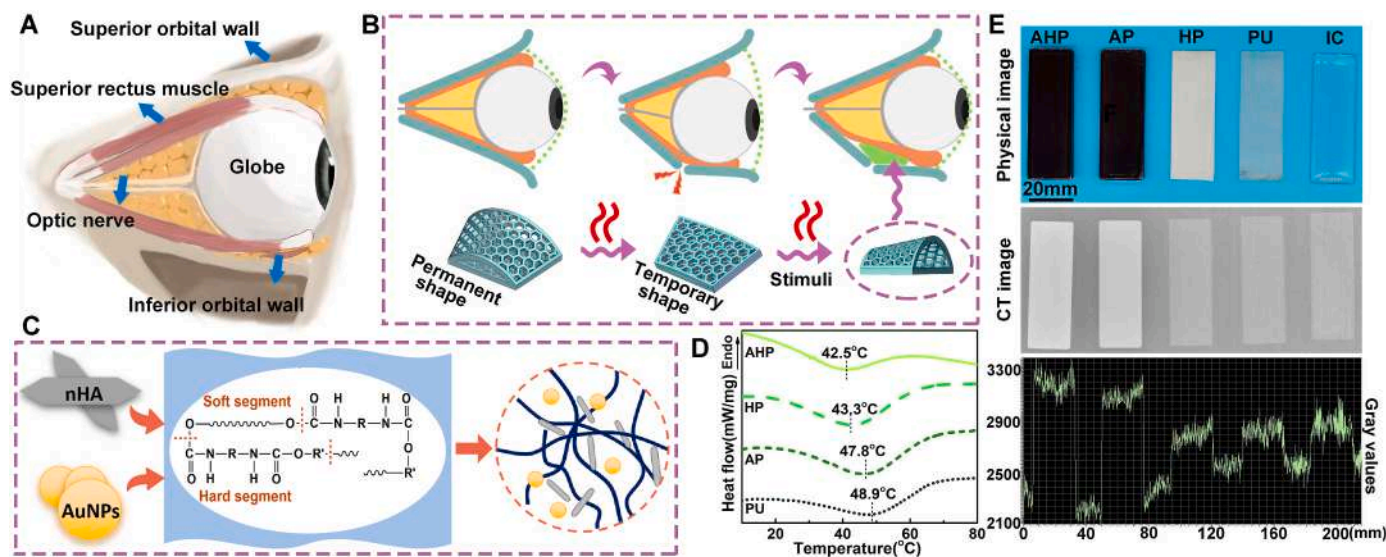


**Fig. 1.** Experimental schematic illustration and material characterization. (A) Schematic illustration of the ocular region. (B) Schematic illustration of the orbital stents before and after implantation for the treatment of enophthalmos. (C) Schematic diagram of preparing the AHP composite. (D) The DSC curves of AHP, AP, HP, PU, and PU. (E) Real photos, CT images, and gray value atlas of AHP, AP, HP, PU, and iodohyalcohol developer.

porosity, the pore structure can be optimized by adjusting the pore geometry and pore size to improve the mechanical properties. Fortunately, four biological structures with good mechanical behavior inspired the design of pore structure, including the *Victoria cruziana* leaf, dragonfly wing, mantis shrimp telson, and honeycomb (Fig. 2A–D) [33–36].

Based on these four biological structures, four bioinspired pore structures of the AHP stent were designed. The square unit, with characteristic dimension  $a$  of the side length, was designed from the vein grid (Fig. 2A). A rectangular unit was designed by rotating and arranging the basic unit. The characteristic dimension  $a$  is the diagonal length

composed of two rectangles (Fig. 2B). The sine unit was designed using sinusoidal geometry with vertical and horizontal arrangements. The characteristic dimension  $a$  is the length of one cycle of a sine function expressed as  $y = \frac{a}{8} \sin(\frac{2\pi x}{a})$ . The honeycomb unit has a characteristic dimension  $a$  of the side length of the hexagon (Fig. 2D). The porosity  $P$  of these units can be calculated from  $a$  and truss thickness  $b$  (Supp. Table S1). Here, a porosity of 60% was selected as the reference value based on the literature [37]. Using the honeycomb unit as an example, three groups of honeycomb mesh plates with the same porosity and different  $(a, b)$  of (1, 0.4), (1.75, 0.7), and (2.5, 1) were deformed into

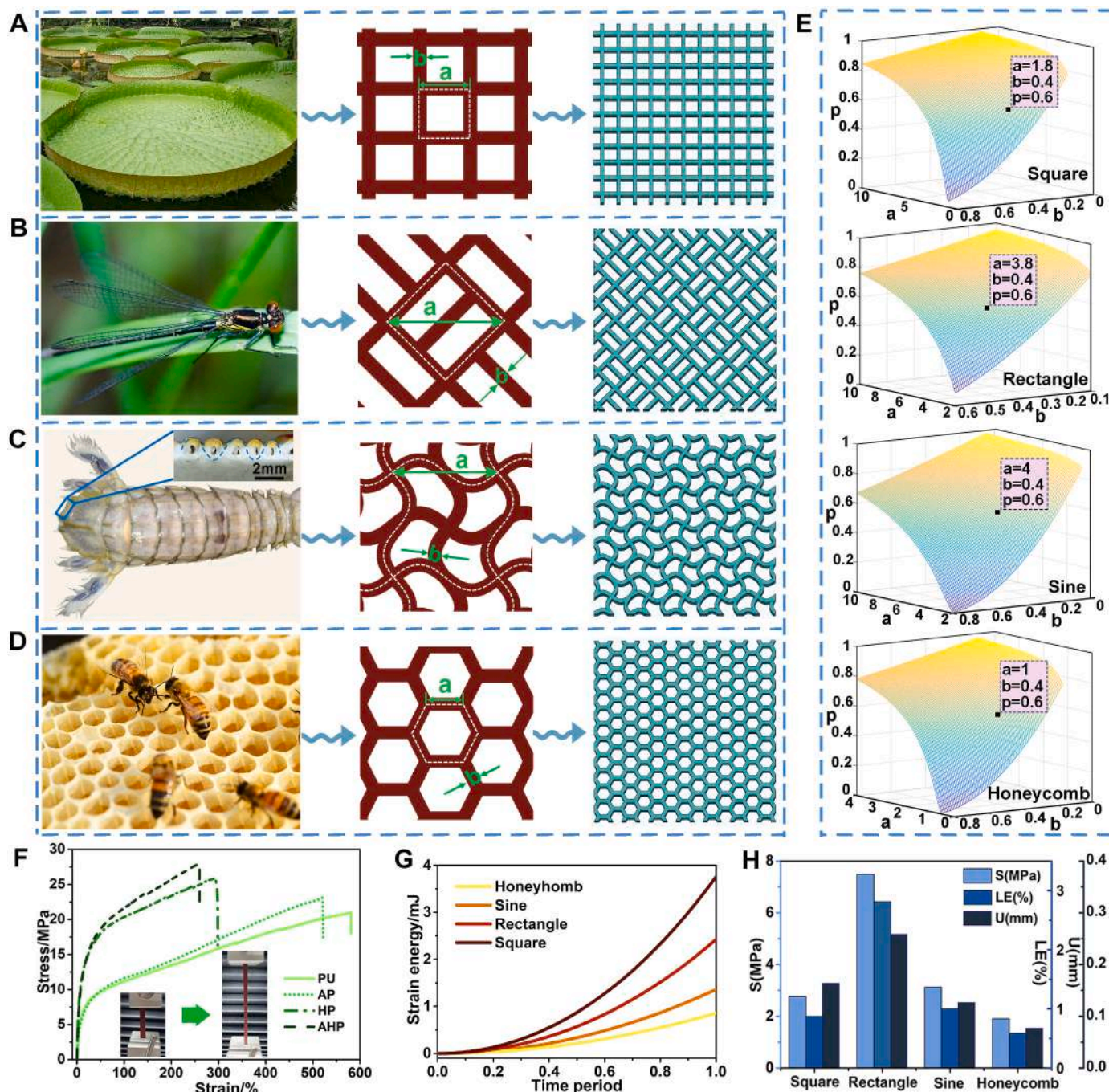


Fig. 2. Process of designing a bionic pore structure. (A) *Victoria cruziana* leaf, the square unit and the square model with a dimension of 20 mm × 20 mm × 2 mm. (B) Dragonfly wing, the rectangle unit and the rectangle model. (C) Mantis shrimp telson and its cross profile [Photo credit: Jiankai Yang, Nanjing University of Aeronautics and Astronautics [35]], the sine unit and sine model. (D) Honeycomb, the honeycomb unit and the honeycomb model. (E) Function relation of porosity  $P$  to  $a$  and  $b$ . (F) Tensile stress-strain curves of PU, AP, HP, and AHP at 37 °C. (G) Strain energy of the four models under the same tensile load were simulated in ABAQUS software. (H) Maximum simulated stress, strain, and displacement values of the four models.

the “U” shape to test the shape recovery performance (Supp. Fig. S6). The plate with (1, 0.4) had a faster response speed and better shape recovery performance. Plates with ( $a$ ,  $b$ ) smaller than (1, 0.4) were prone to fracture of the trusses during printing. Therefore,  $b$  of 0.4 mm is a relatively reasonable size. As shown in the functional image of  $P$  as a function of  $a$  and  $b$  (Fig. 2E), the  $a$  value of each unit can be obtained by confirming the  $P$  and  $b$  values.

To select one unit for the AHP stent, four models with dimensions of 20 mm  $\times$  20 mm  $\times$  2 mm corresponding to the four units were established using SolidWorks 2021 software (Fig. 2A–D). First, uniaxial tensile tests of the PU, AP, HP, and AHP films were conducted at 37 °C to provide the mechanical parameters for simulation (Fig. 2F). PU has excellent toughness, and the elongation at break ( $\epsilon_m$ ) is approximately 600%. Compared with PU,  $\epsilon_m$  of AHP decreases and the tensile strength marginally increases because AuNPs and nHA particles act as “rivets” in the resin matrix. Thereafter, the four models were imported into the ABAQUS CAE software to simulate the mechanical behavior under a tension of 20 N on four sides. As shown in Fig. 2G, the strain energy of the honeycomb model is the lowest, which indicated that the honeycomb structure has stronger structural stability. The maximum simulated stress of square, rectangular, sine, and honeycomb models were 3.90, 3.89, 5.42, and 2.40 MPa, respectively (Supp. Fig. S7). The maximum simulated true strain were 0.83, 2.8, 1, and 0.59%, respectively (Supp. Fig. S8). Maximum simulated displacements are 0.159, 0.1513, 0.224, and 0.088 mm, respectively (Supp. Fig. S9). Comparison of simulated values show that the honeycomb model had the best tensile performance for selection as the pore structure of the AHP stent (Fig. 2H).

### 2.3. Design on outer contour of the AHP stent

The next necessary target was to design an external contour to match

the orbital defect and achieve personalized treatment of enophthalmos. A healthy adult male rabbit weighing approximately 3 kg was selected for CT scanning (Fig. 3A). The CT image shows a wedge-shaped cavity with a left-right height ratio of approximately 3:2 between the superior orbital wall and superior rectus (Fig. 3B). The position was selected to verify the filling capacity of the AHP stent because the superior orbital wall of rabbits occupies the main part of the orbital bone wall and is relatively smooth. The 3D model of the orbital bone was reconstructed using 3-Matic software, and the contour of the superior orbital wall was extracted and highlighted (Fig. 3C). The outer contour of the AHP stent was designed by combining the contour and height ratio of the wedge cavity (Fig. 3D). The hollow design of the AHP stent facilitated connective tissue growth and deformation during MIS. Finally, the AHP stent model was obtained by combining the outer contour with the honeycomb unit, and the detailed size information is shown in Supp. Fig. S10. The AHP stent was constructed using the 3D-Bioplotter (Fig. 3E).

It is crucial to evaluate whether the AHP stent is harmless to surrounding tissues and safely loaded between the superior orbital wall and superior rectus. The maximum pressure exerted on the surrounding tissue by the recovery force was 1 kPa (Supp. Fig. S11), less than the intraocular pressure (IOP) that ranges from 1.3 to 2.8 kPa in human eyes and from 1.3 to 4.5 kPa in rabbits. In addition, the maximum simulated stress in ABAQUS CAE software is approximately 0.9 kPa during shape recovery stage, which is close to the tested value and significantly lower than the IOP range (Supp. Fig. S12), indicating that the recovery force did not influence surrounding tissues. Subsequently, a pressure sensor with a diameter of 8 mm was placed between the superior orbital wall and superior rectus of the rabbit to monitor the pressure before AHP stent implantation. The pressure was monitored steadily at a frequency of 1 Hz/s for 30 min. The same pressure sensor was subsequently pasted onto the curved surface of the AHP stent and implanted into the same

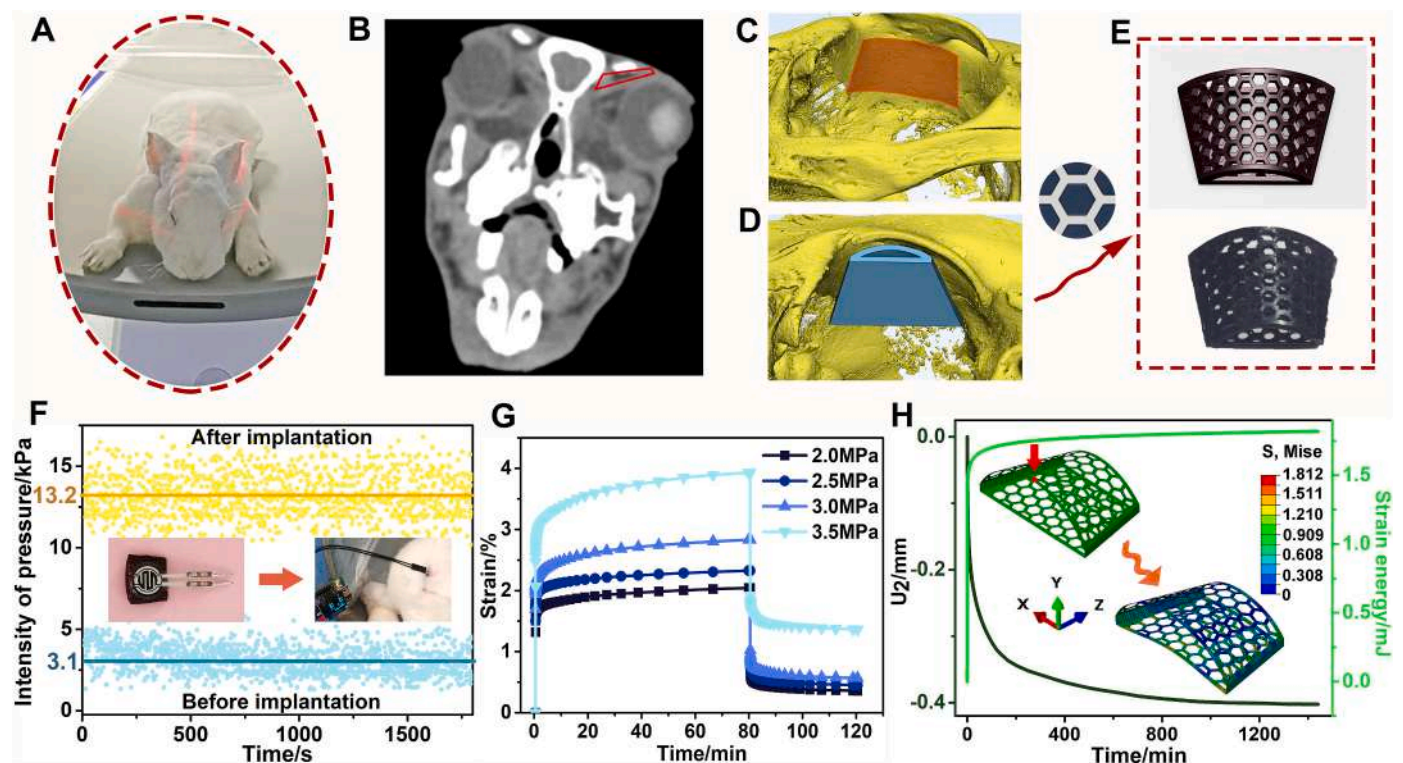


Fig. 3. Process of designing outer contour of the AHP stent. (A) A healthy male rabbit weighing about 3 kg for CT scanning. (B) Cross-sectional CT image of the rabbit head with a wedge-shaped cavity between the superior orbital wall and eyeball. (C) 3D model of the orbital bone reconstructed in 3-Matic software, and the contour of the superior orbital wall with highlight mark. (D) Outer contour of the AHP stent. (E) Model of the AHP stent and the 4D printed AHP stent. (F) Intensity of pressure before and after implantation of the AHP stent between the superior orbital wall and the eyeball. (G) Creep curves of the AHP composite subjected to compression loads of 2, 2.5, 3 and 3.5 MPa at 37 °C. (H) Simulation of stress condition of the AHP stent for 24 h following implantation in ABAQUS software.

location to monitor the pressure following the stent implantation. According to sensor records, the average pressure values between the superior orbital wall and superior rectus before and after AHP stent implantation were 0.37 N and 1.6 N, respectively, far less compared to the maximum compression force of the stent (Supp. Fig. S13), indicating that the stent had sufficient mechanical properties to support the cavity. The pressure intensity at this position was drawn as a scatter diagram (Fig. 3F). Based on the tested pressure intensity, the stress and strain distributions of the AHP stent under a continuous extrusion load following implantation were simulated and analyzed using ABAQUS CAE software. The creep model for the simulation was obtained from the tested creep stress-strain curves under different compression loads (2, 2.5, 3, and 3.5 MPa) (Fig. 3G), which can be expressed by the power-law model:  $\epsilon_{cr} = 8.291^{-4} \cdot \sigma^{1.0637} \cdot t^{0.1436}$  (Supp. Fig. S14). As the curve of displacement U2 in the Y-axis direction (red arrow) of the vertex (red point) shows (Fig. 3H), elastic strain is generated rapidly under pressure following implantation. Subsequently, deformation gradually tended to

be constant. The simulated maximum Mises stress is 1.812 MPa, which is within the elastic range of the AHP composite. It is conclusive that the AHP stent can be safely loaded between the superior orbital wall and superior rectus.

#### 2.4. Cytocompatibility and histocompatibility of the AHP composite

Following implantation, the AHP stent provided temporary support for cell growth to fill the orbital contents [38]. Thus, biodegradability and biocompatibility are necessary for safe implantation of biological stents without secondary removal. The degradation experiments of PU, AP, HP, and AHP films in vitro for eight months (Supp. Fig. S15) showed that the AHP composite broke and disintegrated after 240 d. Cytocompatibility of the AHP composite was evaluated using fibroblast culture in vitro. The fluorescence images of fibroblasts cultured in dishes with PU, AP, and AHP films for 1, 2, and 3 d are shown in Fig. 4A. Living and dead cells were stained green and red, respectively. After 2 d, the

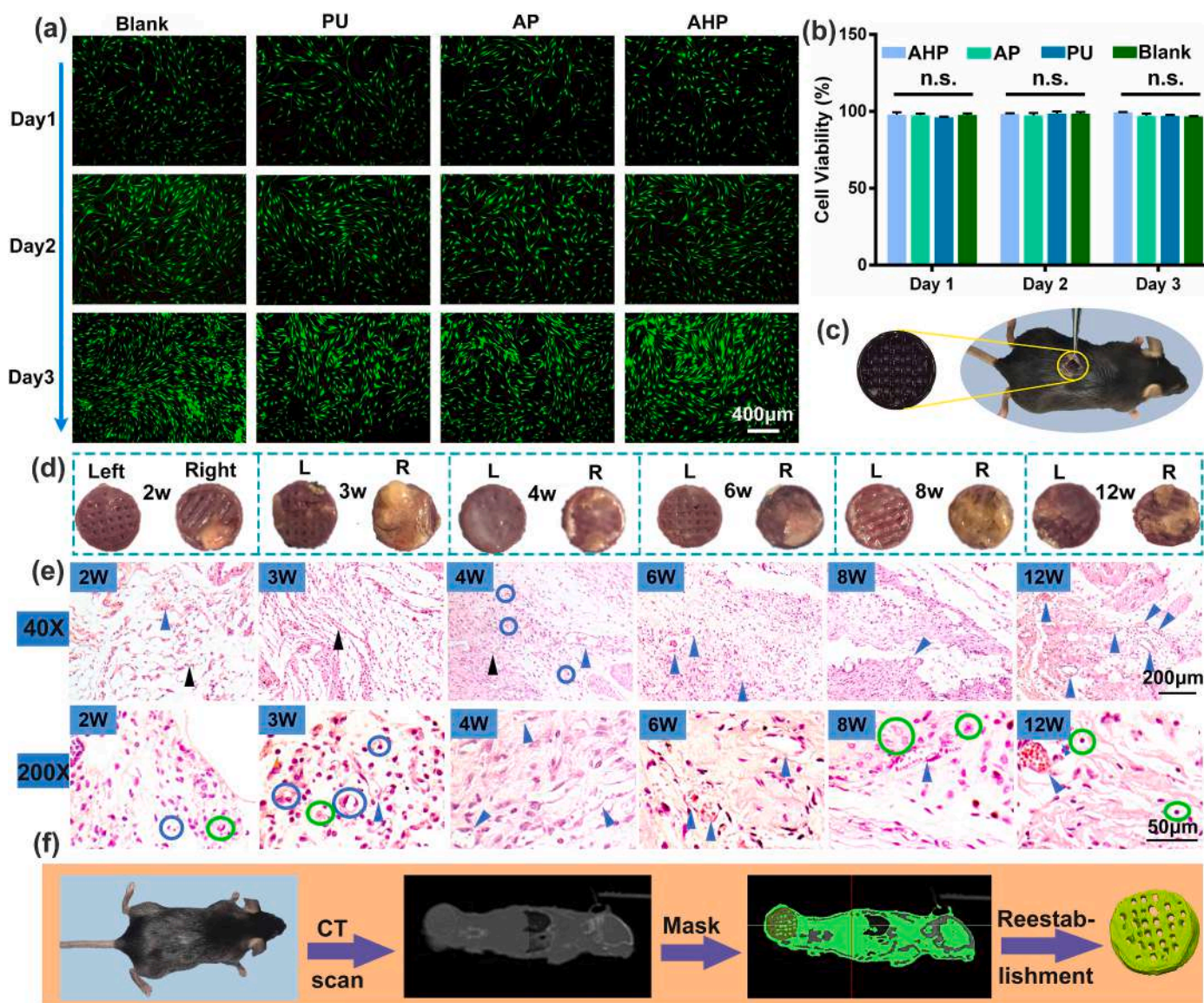


Fig. 4. Cytocompatibility, histocompatibility, and CT-development of the AHP Composite. (A) Fluorescent images of the fibroblast cells cultured in PU, AP, and AHP for 1, 2, and 3 days, living cells: green; dead cells: red. (B) Cell viability of the fibroblast cells cultured in PU, AP, and AHP for 1, 2, and 3 days. (C) Implantation process of the AHP wafers subcutaneously implanted into rats. (D) AHP wafers after different periods of implantation. (E) H&E-stained adjacent tissues of AHP wafers at different time points after implantation, Inflammatory cells: green circles; fibroblast: black arrowheads; newly formed microvessels: blue arrowheads; longitudinally cut blood vessels: blue arrowheads. (F) Reconstruction process of the AHP wafer based on CT images. (For interpretation of the references to colour in this figure legend, the reader is referred to the Web version of this article.)

number of cells increased, and there was no significant difference in cell density among the groups. After 3 d, several dead cells (red) were observed in each group because of increased cell density. The proliferation of cells cultured in the AHP group was higher than that in the PU and AP groups, indicating that nHA and AuNPs could promote cell adhesion and proliferation. The cell viability (Fig. 4B) showed that the cell survival rates were above 90% after 3 d, indicating that the AHP composite had good cytocompatibility.

It is important for an implantable medical device to evaluate inflammatory responses in vivo using histocompatibility experiments. To make the investigation easier to perform, AHP composites were printed as wafers with a porosity of 60% for implantation into female C57BL/6 rats. The diameter and thickness were 8 and 1 mm, respectively (Fig. 4C). This method can simulate the acute and chronic self-preservation responses after foreign body implantation of a porous structure [39]. Following implantation for different periods, tissue encapsulation of these AHP wafers was observed by removing them from the rats (Fig. 4D). In the second week, the wafer was covered with a thin fascia, followed by granulation tissue proliferation, which significantly thickened and peaked in the third week. Tissue hyperplasia was observed on the side in contact with the dorsal muscle (right). In contrast, the skin-side (left) tissue did not become significantly thicker.

The adjacent tissues of AHP wafers were stained with standard hematoxylin-eosin (H&E) and observed under  $40\times$  and  $200\times$  microscope (Fig. 4E). All images at different periods show the generation of a fibrous capsule around the wafers. A foreign body activates the self-protection response of the host, including inflammation, angiogenesis, and fibrosis. Angiogenesis plays an essential role in the proliferative response [40]. At the early stage of implantation (2–3 weeks), AHP wafers were covered with sparse collagen fibers and fibroblasts, accompanied by neovascularization. Only a few inflammatory cells were observed around newly formed microvessels (Fig. 4E, blue circles). After four weeks, the  $200\times$  images show a large number of proliferating fibroblasts and longitudinally cutting blood vessels (blue arrow) in adjacent tissues. After eight weeks, numerous inflammatory cells (green circles) had infiltrated. After 12 weeks, more lymphatic vessels, and blood vessels were distributed in tissues. These results indicated that the AHP composite exhibited good histocompatibility.

To further study CT developability of the AHP composite in vivo, a rat with an AHP wafer implanted subcutaneously in its back was selected for CT scanning. As shown in Fig. 4F, the AHP wafer had a higher CT gray value than the soft tissues. The “Edit Mask” function in Mimics was used to select the image area of the corresponding wafer on each CT slice to establish the multi-layer mask. The multi-layer mask can be reconstructed to the AHP wafer model in 3-Matic 12.0 software. The general shape, size, and pore details can be observed from the reconstructed model, indicating the AHP composite is noteworthy and promising for imaging applications.

### 2.5. Shape memory behavior of the AHP stent in vitro and vivo

It is necessary to investigate the shape memory performance of the AHP stent to realize MIS. Firstly, shape memory performance in vitro was verified in water at  $44^\circ\text{C}$ . The AHP stent was compressed from a hollow permanent shape to a flat temporary shape, and completely recovered the permanent shape within 8 s (Fig. 5A). Through measurements and calculations (Supp. Figs. S5C and D), the  $R_r$  and  $R_f$  of the AHP stent could both reach over 95%.

Shape memory performance in vivo was verified in the orbit of rabbits. Six rabbits weighing 2.5–3 kg were divided into two groups. The right orbit was a surgical case, and the left orbit was a nonsurgical control case. Following intravenous anesthesia and subconjunctival injection, the right orbital rim was exposed by cutting the upper conjunctival fornix. In the first group (group I), the AHP stent with a compressed temporary shape was placed between the upper orbital wall and superior rectus, and the stent did not exceed the upper orbital rim (Fig. 5B). Subsequently, a warm saline solution ( $44^\circ\text{C}$ ) was injected on the AHP stent. Under thermal stimulation, the compressed temporary shape recovered its permanent shape with a larger spatial volume within 36 s (Fig. 5C). In the second group (group II), AHP stents with a compressed temporary shape were directly implanted between the upper orbital wall and superior rectus. No infection or rejection responses occurred in any of the operated animals after surgery for three months.

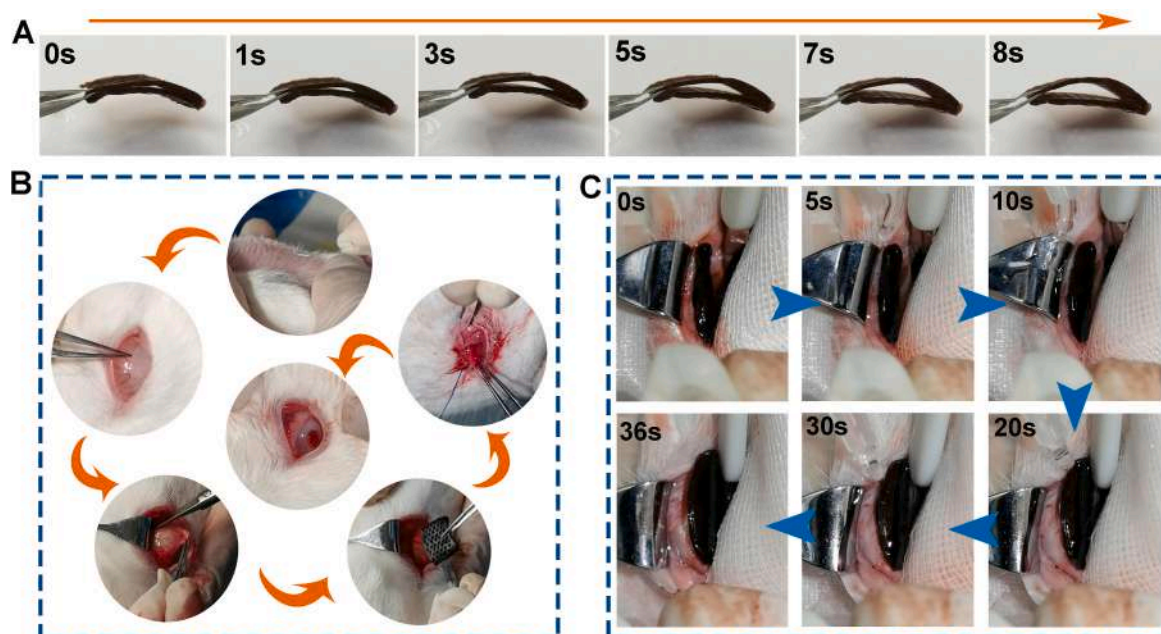


**Fig. 5.** Shape recovery behavior of the AHP stent in vitro and vivo. (A) Shape recovery process of the AHP stent in  $44^\circ\text{C}$  water. (B) Procedure of the AHP stent implantation between the superior orbital wall and the eyeball in experimental rabbits. (C) Shape recovery process of the AHP stent under the stimulation of saline solution ( $44^\circ\text{C}$ ) in the orbit of the rabbit.

2.6. Volume filling

The key to the treatment of enophthalmos is filling the orbital coloboma to restore orbital volume. Therefore, the measurement of volume variation after AHP stent implantation is essential to evaluate surgical results [41]. Based on the CT imaging technique, orbital volumetry (OV) provides an appropriate characterization for defining the size of implants to increase accuracy and shorten surgical procedures [42,43]. There are two main methods of OV: planimetry and stereology. Planimetry is the summation of a series of manually defined areas of CT slices. Stereology has been used to measure orbital volume based on statistical point counting [44–46].

Six rabbits weighing 2.5–3 kg were divided into groups III and IV, and CT scans were performed prior to implantation. Medpors (08.510.120s, Synthes GmbH, Switzerland) and absorbable bone plates

(abs-plates) (FRF-1013, Inion Oy, Finland) were implanted into the right eye of rabbits in groups III and IV, respectively. The Medpors and abs-plates were cut to the same size and shape as the compressed AHP stent. They all had a thickness of 2 mm and volume of 240 mm<sup>3</sup>. The orbital parts of the rabbits in groups I, II, III, and IV before and after implantation all can be split into approximately 20 CT slices with a thickness of 1 mm. As shown in Fig. 6A, taking the line between the mandible and nasal septum as a reference (blue dotted line), the CT slices before and after implantation can be matched one by one. It is difficult for Medpor and Abs-plates to be observed in CT images. The AHP stent has better radiographic development to be seen more clearly. The CT images of the recovered AHP stent clearly show no collapse or fracture, which proves the feasibility of the AHP stent for volume filling.

Using planimetry, the overall volume difference can be calculated by adding the orbital area (red dotted line) of each CT slice. As shown in

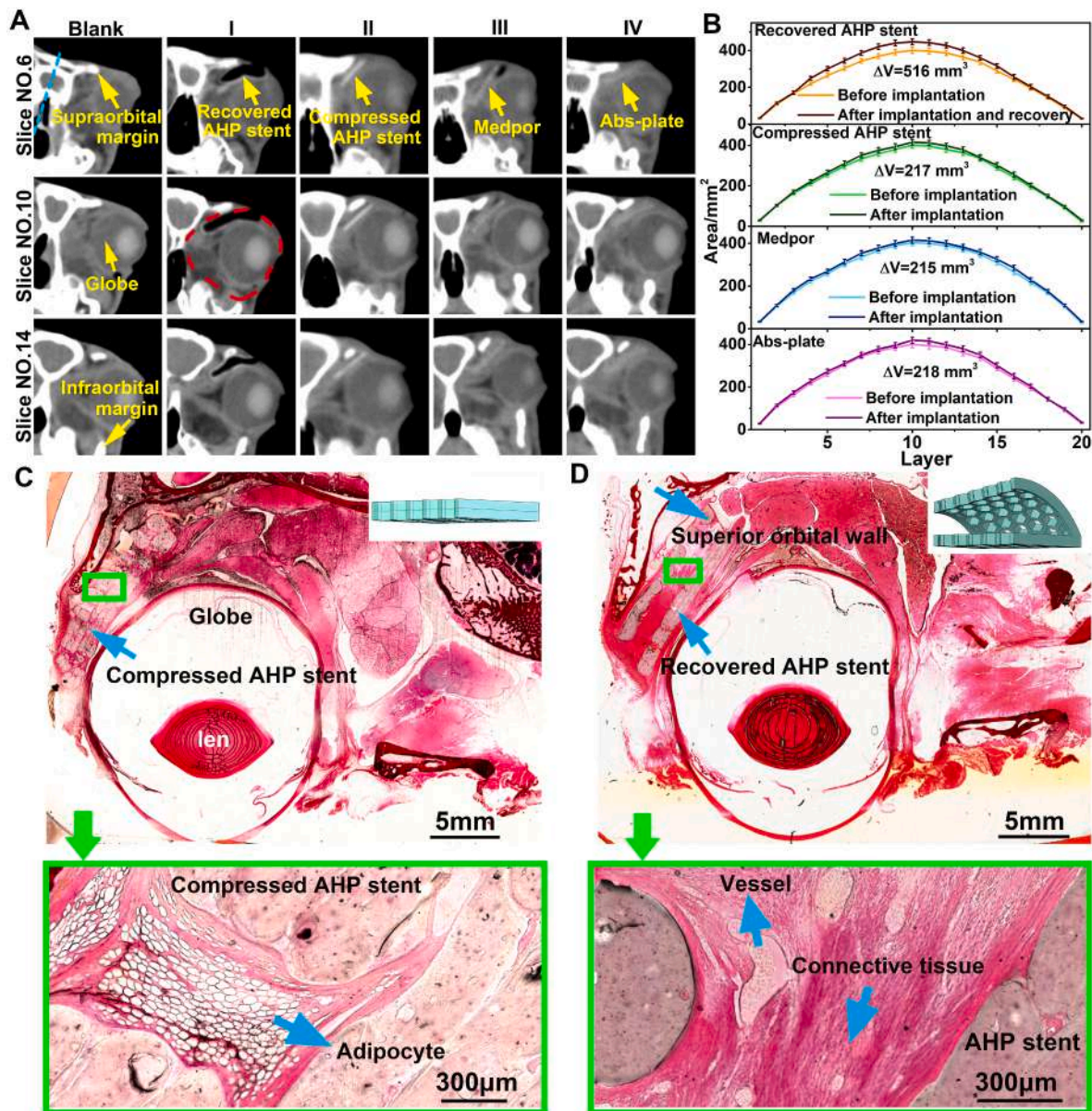


Fig. 6. Orbital volume changes of AHP compared with commercial implants. (A) CT slices of the intraorbital area without implant, after implantation with the recovered AHP stent, the compressed AHP stent, Medpor and Abs-plate. (B) Orbital volume increment caused by the implantation of the AHP stent through shape recovery, the compressed AHP stent, the Medpor and the Abs-plate. (C) Lower magnification showing the location of the compressed AHP stent, superior orbital wall and globe, higher magnification showing the soft tissue in the green wireframe. (D) Lower magnification showing the location of the recovered AHP stent, superior orbital wall and globe, higher magnification showing the soft tissue in the green wireframe. (For interpretation of the references to colour in this figure legend, the reader is referred to the Web version of this article.)

Fig. 6B, the volume increments caused by the implantation of the compressed AHP stent, Medpor, and Abs-plate are 217, 215, and 218 mm<sup>3</sup>, respectively, which are all smaller than the actual implant volume (240 mm<sup>3</sup>). The volume filling rates, defined as the ratio of the orbital volume increment to the implant volume, were 90.4, 89.6, and 90.8%, respectively. In contrast, the volume difference caused by shape recovery of the AHP stent through the shape memory effect after implantation reached 516 mm<sup>3</sup>, offering a volume filling of nearly 150% more than that of the other three groups. Moreover, the volume filling rate of the recovered stent was more than 200%, indicating that the 4D printed stent with shape memory effect is important for efficient filling of orbital defects and personalized treatment of enophthalmos.

Three months after implantation, the contents of the entire right orbital in groups I and II, including the orbital walls of rabbits, were excised and cut into 50- $\mu$ m coronal slices. The direction and location of the coronal section relative to the AHP stent are shown in the upper-right corner of Fig. 6C and D. Histopathological slides were examined for the location of recovered and compressed AHP stents in the orbital tissue. As shown in Fig. 6C, the compressed AHP stent was surrounded by soft tissue including a small number of lymphocytes and fibrotic scars. The cavity volume of the compressed AHP stent was small. As the higher magnification image in the green wireframe shows, numerous fat cells grow into honeycomb pores, while new vessels are rarely seen. As shown in Fig. 6D, the recovered AHP stent with a greater cavity volume was wrapped by connective tissue and grew vascular buds and connective tissue in the cavity. These vascular buds provide a pipeline for nutrients uptake, tissue oxygenation, and cell transport to promote tissue regeneration. There were no foreign body rejection or infection responses after the three-month implantation of the recovered or compressed AHP stents, which indicated that the AHP stent has good biosafety and functionality as a medical device for filling volume.

### 3. Conclusion

In summary, a 4D printed orbital stent with CT developability was fabricated for efficient filling of orbital defects and personalized treatment of enophthalmos. The results showed that AuNPs and nHA endow the AHP composite with excellent developability compared with the matrix under X-ray contrast examination. Combining the bionic honeycomb pore structure and the outer contour gained from CT reconstruction technology, the 4D printed AHP stent still had good mechanical properties to support the orbital tissue. Moreover, the AHP stent restored its shape within 8 s in water at 44 °C. Following implantation of the 4D printed AHP stent in the orbit to the rabbit via MIS, the compressed temporary shape of the stent successfully recovered to a permanent shape under thermal stimulation. With implants of the same shape, size, and volume, the AHP stent through shape recovery can offer a volume filling of nearly 150% more than that of the compressed AHP stent, Medpor, or Abs-plate. The three-month follow-up showed good postoperative results of orbital tissue growth into the stent. Thus, the AHP stent can be a promising medical device for the personalized treatment of enophthalmos. The AHP composite, as a type of biomaterial, has considerable potential for visual, personalized, and minimally invasive treatment in the biomedical field and is not limited to the treatment of enophthalmos.

## 4. Materials and methods

### 4.1. Preparation of the PU emulsion

10 g polycaprolactone diol (PCL-OH, Hunan Juren Chemical Technology Co., LTD, China) with a molecular weight of 2000 was added into a three-mouth flask and vacuumed for 3 h at 120 °C. Then, 2.6 g hexamethyldiisocyanate (HDI, Aladdin Reagent (Shanghai) Co., LTD, China) and 0.5 g dibutyltin dilaurate (Aladdin Reagent (Shanghai) Co., LTD, China) were added for a 3-h reaction at 90 °C in a nitrogen

atmosphere. The reaction temperature was then cooled to 70 °C, and 0.9 g 1, 4-butandiol (BDO, Aladdin Reagent (Shanghai) Co., LTD, China) was added for a 2-h reaction, the viscosity was adjusted with acetone. After cooled to 40 °C, the mixture was neutralized with triethylamine (TEA, Aladdin Reagent (Shanghai) Co., LTD, China) and emulsified with ice water. Finally, the PU emulsion was obtained by removing acetone through vacuum distillation.

### 4.2. Preparation of the composites

Step one, 4 g AuNPs colloid (0.1 wt%, Xuzhou Jiechuang New Materials Technology Co., LTD, China) was added drop by drop into 10 g PU emulsion (20 wt%). Subsequently, AP mixture was obtained after mechanical stirring for 2 h. Step two, 0.2 g nHA powder (Xi'an Ruilin Biological Technology Co., LTD, China) was added into 5 g deionized water, and stirred for 2 h at room temperature, then endured ultrasonic concussion for 3 h to obtain evenly dispersed nHA suspension. Step three, the AHP mixture was obtained by slowly adding the nHA suspension into the AP mixture and stirred for 2 h. The AHP membrane was obtained by drying the mixture in a 60 °C vacuum drying box for 12 h. The HP membrane was obtained by directly dropping the nHA suspension into PU emulsion and then stirred for 2 h and dried for 12 h.

### 4.3. Mechanical property tests

Uniaxial tensile tests were performed according to ASTM D638. The samples were cut into dumbbell shapes with 115 mm  $\times$  6 mm  $\times$  1 mm. All tensile tests were conducted on a Zwick 010 (Zwick GmbH & Co. KG, Germany) at the temperature of 37 °C with a preload of 0.1 N and a loading speed of 5 mm/min. In each case, five samples were tested to obtain an average value. The compressive creep experiments of the AHP composite under four loading values (2, 2.5, 3 and 3.5 MPa) at 37 °C were conducted on a dynamic thermomechanical analyzer (Q800, TA Instruments, USA). All the samples were cut mechanically into cylinder with dimensions of 5 mm  $\times$  5 mm, and the loading durations were 160 min.

### 4.4. In vitro degradation

PU, AP, HP and AHP membranes were cut into rectangular samples with a dimension of 40 mm  $\times$  10 mm  $\times$  0.5 mm, which were weighed, put into erlenmeyer flasks and numbered (Fig. S15). The samples were put into sealed erlenmeyer flasks filled with Hanks solution (Fuzhou Feijing Biological Technology Co., Ltd, China), and then the flasks were placed into a shaker incubator with a temperature of 37 °C. The samples were taken out at intervals, washed with deionized water, and vacuum-dried to constant weight. After recording the mass, the samples were put back into the erlenmeyer flasks with new Hanks solution. The experiment lasted eight months. The percentage of weight loss ( $\omega_l$ ) was calculated by

$$\omega_l = \frac{m(t) - m_0}{m_0} \times 100\% \quad (1)$$

where  $m(t)$  is the weight of the specimen on time  $t$  after degradation and  $m_0$  is the original weight before degradation.

### 4.5. Simulation in ABAQUS

The simulation methods of the four models (square, rectangle, sine, honeycomb) under tensile load: in the material behavior, the mechanics were set as hyperelastic, and the experimental data were equiaxial test data obtained from the tensile test of the AHP composite. The third-order Ogden hyperelastic constitutive model was adopted for strain potential energy. The density was  $1.3 \times 10^{-9}$  t/mm<sup>3</sup>. The grids of the four models were all divided into hexahedron cells. The load was to

apply tension force (20 N) perpendicular to the four edges of the model.

The simulation method of the AHP stent under compressed load: the outer surface of the AHP stent model was extracted in HyperWorks2019 software and divided into quadrilateral grids. The grid model was imported into ABAQUS CAE Software, and the material behavior was set as creep and elastic. The creep method was Time hardening. The form and the Section type were set as shell and homogeneous, respectively. Step1 was set as static, general. Step2 was set as viscous. The loading was the pressure. The intensity of pressure on curved surface of the AHP stent model was set as 12 kPa, and the one on the plane was set as 18 kPa.

#### 4.6. Fabrication of structures

The AHP wafer and AHP stent fabrication was realized by the high-temperature printing mode of 3D-Bioplotter (3D-Bioplotter, EnvisionTEC, USA). Initially, assemble the barrel and the extrusion needle with a diameter of 0.1 mm, and a rubber gasket was sealed at the coupling. Secondly, film samples were cut into fragments and added into the barrel, then preheated at 170 °C until the materials can be smoothly extruded. Afterward, the 3D model was cut into slices with a height of 0.08 mm in Perfactory RP software. Subsequently, the printing parameters were defined as: barrel temperature was 180 °C, extrusion pressure was 2 Bar, printing speed was 5 mm/s, shell thickness was 0.2 mm, the infill type was linear with an infill spacing of 0.1 mm.

#### 4.7. Shape memory behaviors

The AHP membranes with dimensions of 40 mm × 5 mm × 0.5 mm were heated in 44 °C water and bent into “U” shape. After cooling, the temporary shape was fixed. Then, the AHP membranes were actuated in 44 °C water. For the AHP stent, the sizes of  $h_a$  ( $h_0$ ) were measured before the test. Subsequently, the AHP stent was compressed into a flat temporary shape in 44 °C water. The temporary shape was fixed upon cooling, and the size of  $h_l$  was measured. Then the AHP stent with temporary shape was put into 44 °C water, while a camera was used to record the recovery process of the stent.

#### 4.8. Cell culture and cytotoxicity assay

The primary fibroblasts were cultured in Dulbecco's modified Eagle's medium containing 10% calf serum, 100 U/ml penicillin/streptomycin in a 37 °C humidified atmosphere with 5% CO<sub>2</sub>. The membranes of PU, AP and AHP with a thickness of 0.5 mm were cut into small discs with a diameter of 5 mm. The discs were sequentially sterilized with 75% absolute ethanol for 3 h, washed with phosphate buffer saline three times, and then exposed to ultraviolet light for 8 h. After sterilization, about 10<sup>5</sup> primary fibroblasts were seeded at the bottom of each well, co-incubated with the PU, AP and AHP discs, respectively. Calcein/PI Cell Viability/Cytotoxicity Assay Kit (C2015, Beyotime Co., Ltd, China) was deployed in a humidified incubator with 5% CO<sub>2</sub> at 37 °C. The fibroblast viability of each sample was quantified at days 1, 2 and 3 post-seeding to analyze the cytotoxicity. Living cells (stained green) and dead cells (stained red) were observed and captured by fluorescence microscopy (Olympus Corporation, Tokyo, Japan). The stained images were imported into ImageJ software, and the living cells and dead cells were counted and the percentages of living cells were calculated.

#### 4.9. In vivo histocompatibility analysis

The experiments in mice were approved by the Medical Ethics Committee of the 2nd Affiliated Hospital of Harbin Medical University. The approval document number of ethical review is SYDW2021-110. A total of 18 female C57BL/6 rats weighing about 25–28 g were randomly allocated into six groups. After anesthetized, the AHP wafer was implanted subcutaneously. Subsequently, the rats were euthanized and prepared for evaluation at 2, 3, 4, 6, 8 and 12 weeks post-surgery. The

wafers and adjacent tissues were collected for gross observation and histological analysis at each time point. After fixing in 4% paraformaldehyde overnight at 4 °C and dehydrated, tissues were embedded in paraffin. The adjacent tissues were cut longitudinally into 4 μm thick slices by a tissue slicer (RM2235, Leica, Germany) and mounted on glass slides. Sections were observed with a hematoxylin-eosin staining kit (WLA051A, China) by using a light microscopic examination (DP73, OLYMPUS, Japan).

#### 4.10. Operation of AHP stent implantation

This animal experiment was performed under the guidelines of Medical Ethics Committee of the 2nd Affiliated Hospital of Harbin Medical University. The approval document number of ethical review is SYDW2021-110. After surgical sterilization, the subject rabbits were anesthetized by intravenous administration (10% chloral hydrate, 2.5–3 ml/kg). Subsequently, the right orbit was received subconjunctival injection of 2% lidocaine. The upper conjunctival fornix was cut open. The Tenon's sacs were blunt dissection until the right orbital rim was exposed, the AHP stent was implanted between the upper orbital wall and the superior rectus. The surgical wound was flushed by saline solution dissolving 20000 units of gentamicin. The conjunctiva and the subconjunctival tissue layer were sutured with absorbable threads. Mixed (tobramycin and dexamethasone) ophthalmic ointment was administrated over eye. Ofloxacin eye drop was given three times per day for a week.

#### 4.11. CT scanning

CT scanning on rats and rabbits: after intravenous anesthesia with 10% chloral hydrate (2.5–3 ml/kg), the rats or rabbits were placed in a prone position. Subsequently, a 16-slice spiral CT scan was performed with the scan conditions set as slice thickness 1 mm, scan voltage 140 kV, tube current 140 mA, rotation time 1 s and pitch 0.63. Precise CT scan for the orbital bone of the rabbit: the orbital bone of a healthy adult rabbit weighing 2.5 kg was taken and performed coronal scan by using MicroCT (scanco μ35). The thickness of the scan layer was 18.5 μm.

#### 4.12. Orbital volumetry

DICOM format files were imported into Mimics Research 20.0. The orbital boundary is starting from the supraorbital margin, extending along the superior orbital wall to the infraorbital margin. Based on the function “Measure Area” in Mimics, the area of orbital part was delineated three times of each horizontal-section slice to ensure the reliability. The three intraorbital areas obtained from each slice were averaged to obtain the final area value. The volume ( $V$ ) of the segmented orbital cavity was calculated by:

$$V = \sum_i^m (T a_i) \quad (2)$$

where  $T$  is the slice thickness,  $a_i$  is the manually selected area in slice  $i$ , and  $m$  is the total number of slices.

#### 4.13. Coronal section of whole orbit

The rabbits of group I and group II were euthanized for 3 months after implantation. The whole right orbital content including orbital walls was excised and placed in 4% paraformaldehyde. The harvested right orbits were submitted to the Shanghai Pengli Biology Corporation. The orbit specimens were dehydrated, cleared with gradient alcohol and xylene, then infiltrated manually and embedded in paraffin. 50-μm coronal sections of the embedded orbital block were obtained with EXKAT grinding system. The sections were stained with hematoxylin-eosin solution. The histopathologic slides were reviewed and

examined with routine light microscopy.

## Funding

J.L. thank the National Natural Science Foundation of China (11632005) and the Fundamental Research Funds for the Central Universities (Grant No: IR2021106) for financial support. H.Y. thank the National Natural Science Foundation of China (82070956) for financial support. Y.L. thank the National Natural Science Foundation of China (12072094) and the Fundamental Research Funds for the Central Universities (Grant No: IR2021232) for financial support.

## Author contributions

J.L. and H.Y. conceived and designed the experiments. Y.D. and F.Z. performed all the characterization tests of material, the construction of the model and simulation. B.Y., J.S., and Y.D. performed all animal implantation experiments and CT imaging tests. S.Z. and Y.Z. performed cell culture, cytotoxicity test and histocompatibility testing. Y.D., B.Y. and S.Z. undertook data analyses. Y.J. undertook project administration. Y.D. wrote the original manuscript. J.L., H.Y. and F.Z. validated test results. F.Z., J.L., H.Y. and B.Y. performed review and editing for manuscript.

## Declaration of competing interest

The authors declare that they have no known competing financial interests or personal relationships that could have appeared to influence the work reported in this paper.

## Data availability

The data that has been used is confidential.

## Acknowledgment

We acknowledge the experimental and technical support of the Centre for Composite Materials, Harbin Institute of Technology. We thanks to the assistance of the Department of ophthalmology, the 2nd affiliated hospital of Harbin medical university. We give thanks to the Heilongjiang Touyan Innovation Team Program for providing the technological guidance.

## Appendix A. Supplementary data

Supplementary data to this article can be found online at <https://doi.org/10.1016/j.biomaterials.2022.121886>.

## References

- [1] Y. Xie, Y. Meng, W. Wang, E. Zhang, J. Leng, Q. Pei, Bistable and reconfigurable photonic crystals—electroactive shape memory polymer nanocomposite for ink-free rewritable paper, *Adv. Funct. Mater.* 28 (2018), 1802430, <https://doi.org/10.1002/adfm.201802430>.
- [2] Y. Zhang, N. Zhang, H. Hingorani, N. Ding, D. Wang, C. Yuan, B. Zhang, G. Gu, Q. Ge, Fast-response, stiffness-tunable soft actuator by hybrid multimaterial 3D printing, *Adv. Funct. Mater.* 29 (2019), 1806698, <https://doi.org/10.1002/adfm.201806698>.
- [3] Y. Liu, W. Zhang, F. Zhang, X. Lan, J. Leng, S. Liu, X. Jia, C. Cotton, B. Sun, B. Gu, T.W. Chou, Shape memory behavior and recovery force of 4D printed laminated Miura-origami structures subjected to compressive loading, *Compos. B Eng.* 153 (2018) 233–242, <https://doi.org/10.1016/j.compositesb.2018.07.053>.
- [4] G. Zhang, Q. Zhao, W. Zou, Y. Luo, T. Xie, Unusual aspects of supramolecular networks: plasticity to elasticity, ultrasoft shape memory, and dynamic mechanical properties, *Adv. Funct. Mater.* 26 (2016) 931–937, <https://doi.org/10.1002/adfm.201504028>.
- [5] X. Gong, F. Xie, L. Liu, Y. Liu, J. Leng, Electro-active variable-stiffness corrugated structure based on shape-memory polymer composite, *Polymers* 12 (2020) 387, <https://doi.org/10.3390/polym12020387>.
- [6] R. Liang, H. Yu, L. Wang, N. Wang, B.U. Amin, NIR light-triggered shape memory polymers based on mussel-inspired iron-catechol complexes, *Adv. Funct. Mater.* 31 (2021), 2102621, <https://doi.org/10.1002/adfm.202102621>.
- [7] Y. Zhou, J. Tan, D. Chong, X. Wan, J. Zhang, Rapid near-infrared light responsive shape memory polymer hybrids and novel chiral actuators based on photothermal W18O49 nanowires, *Adv. Funct. Mater.* 29 (2019), 1901202, <https://doi.org/10.1002/adfm.201901202>.
- [8] C. Lin, J. Lv, Y. Li, F. Zhang, J. Li, Y. Liu, J. Leng, 4D-printed biodegradable and remotely controllable shape memory occlusion devices, *Adv. Mater. Technol.* 29 (2019), 1906569, <https://doi.org/10.1002/adfm.201906569>.
- [9] W. Zhao, F. Zhang, J. Leng, Y. Liu, Personalized 4D printing of bioinspired tracheal scaffold concept based on magnetic stimulated shape memory composites, *Compos. Sci. Technol.* 184 (2019), 107866, <https://doi.org/10.1016/j.compscitech.2019.107866>.
- [10] W. Wang, L. Du, Y. Xie, F. Zhang, P. Li, F. Xie, X. Wan, Q. Pei, J. Leng, N. Wang, Bioinspired four-dimensional polymeric aerogel with programmable temporal-spatial multiscale structure and functionality, *Compos. Sci. Technol.* 206 (2021), 108677, <https://doi.org/10.1016/j.compscitech.2021.108677>.
- [11] C. Xu, F. Liu, A. Bugarin, Y. Hong, Synthesis and characterization of a conductive, biodegradable polyurethane elastomer, *Front. Bioeng. Biotechnol.* 4 (2016), 02511, <https://doi.org/10.3389/conf.FBIOE.2016.01.02511>.
- [12] R. Xie, J. Hu, O. Hoffmann, Y. Zhang, F. Ng, T. Qin, X. Guo, Self-fitting shape memory polymer foam inducing bone regeneration: a rabbit femoral defect study, *BBA-Gen. Subjects* 1862 (2018) 936–945, <https://doi.org/10.1016/j.bbagen.2018.01.013>.
- [13] B. Zhang, H. Li, J. Cheng, H. Ye, A.H. Sakhaei, C. Yuan, P. Rao, Y.F. Zhang, Z. Chen, R. Wang, X. He, J. Liu, R. Xiao, S. Qu, Q. Ge, Mechanically robust and UV-curable shape-memory polymers for digital light processing based 4D printing, *Adv. Mater.* 33 (2021), 2101298, <https://doi.org/10.1002/adma.202101298>.
- [14] H. Cui, C. Liu, T. Esworthy, Y. Huang, Z. Yu, X. Zhou, H. San, S.J. Lee, S.Y. Hann, M. Boehm, M. Mohiuddin, J.P. Fisher, L.G. Zhang, 4D physiologically adaptable cardiac patch: a 4-month in vivo study for the treatment of myocardial infarction, *Sci. Adv.* 6 (2020), <https://doi.org/10.1126/sciadv.abb5067> eabb5067.
- [15] P. Wang, G. Zhang, J. Liu, S. Nie, Y. Wu, S. Deng, G. Fang, J. Zhou, J. Song, J. Qian, P. Pan, Q. Zhao, T. Xie, Light-coded digital crystallinity patterns toward bioinspired 4D transformation of shape-memory polymers, *Adv. Funct. Mater.* 30 (2020), 2000522, <https://doi.org/10.1002/adfm.202000522>.
- [16] S. Miao, H. Cui, M. Nowicki, L. Xia, X. Zhou, S. Lee, W. Zhu, K. Sarkar, Z. Zhang, L. G. Zhang, Stereolithographic 4D bioprinting of multiresponsive architectures for neural engineering, *Adv. Biosys.* 2 (2018), 1800101, <https://doi.org/10.1002/adbi.201800101>.
- [17] H. Chen, C. Pan, A. Leow, P. Tsay, C. Chen, Evolving concepts in the management of orbital fractures with enophthalmos: a retrospective comparative analysis, *Formos. J. Surg.* 49 (2016) 1–8, <https://doi.org/10.1016/j.fjs.2015.06.002>.
- [18] E.S. Lee, J.W. Han, H.S. Choi, J.W. Jang, S.J. Kim, S.Y. Jang, Differences in interpupillary fissure measurement in patients with unilateral enophthalmos resulting from orbital wall fractures, *J. Cranio. Maxill. Surg.* 45 (2017) 690–693, <https://doi.org/10.1016/j.jcms.2017.02.017>.
- [19] A. Ebrahimi, M.H. Kalantar Motamedi, H.R. Rasouli, N. Naghdi, Enophthalmos and orbital volume changes in zygomaticomaxillary complex fractures: is there a correlation between them? *J. Oral Maxillofac. Surg.* 77 (2019) 131–134, <https://doi.org/10.1016/j.joms.2018.08.028>.
- [20] L.M. Cohen, L.A. Habib, M.K. Yoon, Post-traumatic enophthalmos secondary to orbital fat atrophy: a volumetric analysis, *Orbit* 1 (2019) 1–6, <https://doi.org/10.1080/01676830.2019.1691607>.
- [21] C. Sentucq, M. Schlund, B. Bouet, M. Garms, J. Ferri, T. Jacques, R. Nicot, Overview of tools for the measurement of the orbital volume and their applications to orbital surgery, *J. Plast. Reconstr. Aes.* 74 (2021) 581–591, <https://doi.org/10.1016/j.bjps.2020.08.101>.
- [22] J. Choi, S.W. Park, J. Kim, J. Park, J.S. Kim, Predicting late enophthalmos: differences between medial and inferior orbital wall fractures, *J. Plast. Reconstr. Aes.* 69 (2016) 238–244, <https://doi.org/10.1016/j.bjps.2016.08.004>.
- [23] C.Y. Kim, B.J. Jeong, S.Y. Lee, J.S. Yoon, Comparison of surgical outcomes of large orbital fractures reconstructed with porous polyethylene channel and porous polyethylene titan barrier implants, *Ophthalmic Plast. Reconstr. Surg.* 28 (2012) 176–180, <https://doi.org/10.1097/IOP.0b013e3182467c4a>.
- [24] T.L. Kersey, S. Ng, P. Rosser, B. Sloan, R. Hart, Orbital adherence with titanium mesh floor implants: a review of 10 cases, *Orbit* 32 (2013) 8–11, <https://doi.org/10.3109/01676830.2012.736597>.
- [25] H. Zhou, J. Lee, Nanoscale hydroxyapatite particles for bone tissue engineering, *Acta Biomater.* 7 (2011) 2769–2781, <https://doi.org/10.1016/j.actbio.2011.03.019>.
- [26] H. Lusic, M.W. Grinstaff, X-ray-computed tomography contrast agents, *Chem. Rev.* 113 (2013) 1641–1666, <https://doi.org/10.1021/cr200358s>.
- [27] F. Kiessling, *Small Animal Imaging: Basics and Practical Guide*, first ed., Springer, Berlin, 2011.
- [28] P. Li, D. Li, L. Zhang, G. Li, E. Wang, Cationic lipid bilayer coated gold nanoparticles-mediated transfection of mammalian cells, *Biomaterials* 29 (2008) 3617–3624, <https://doi.org/10.1016/j.biomaterials.2008.05.020>.
- [29] J.J. Grisel, J.H. Atkins, D.J. Fleming, R.B. Kuppersmith, Clinical evaluation of a bioresorbable implant for medialization of the middle turbinate in sinus surgery, *Int. Forum Allergy Rh.* 1 (2015) 33–37, <https://doi.org/10.1002/alr.20001>.
- [30] C. Flege, F. Vogt, S. Hoges, L. Jauer, M. Borinski, V.A. Schulte, R. Hoffmann, R. Poprawe, W. Meiners, M. Jobmann, K. Wissenbach, R. Blindt, Development and characterization of a coronary polylactic acid stent prototype generated by

- selective laser melting, *J. Mater. Sci. Mater. Med.* 24 (2013) 241–255, <https://doi.org/10.1007/s10856-012-4779-z>.
- [31] D. Yoo, New paradigms in hierarchical porous scaffold design for tissue engineering, *Mat. Sci. Eng C-Mater.* 33 (2013) 1759–1772, <https://doi.org/10.1016/j.msec.2012.12.092>.
- [32] J. Li, M. Chen, X. Fan, H. Zhou, Recent advances in bioprinting techniques: approaches, applications and future prospects, *J. Transl. Med.* 14 (2016) 271, <https://doi.org/10.1186/s12967-016-1028-0>.
- [33] R. Yuan, H. Lei, Discuss on the new form of vein of lotus leaves, *Friend of Science Amateurs* 5 (2008) 155.
- [34] L. Ren, X. Li, Functional characteristics of dragonfly wings and its bionic investigation progress, *Sci. China Technol. Sci.* 56 (2013) 884, <https://doi.org/10.1007/s11431-013-5158-9>.
- [35] J. Yang, D. Gu, K. Lin, Y. Yang, C. Ma, Optimization of bio-inspired bi-directionally corrugated panel impact-resistance structures: numerical simulation and selective laser melting process, *J. Mech. Behav. Biomed.* 91 (2018) 59, <https://doi.org/10.1016/j.jmbbm.2018.11.026>.
- [36] J.M. Korde, M. Shaikh, B. Kandasubramanian, Bionic prototyping of honeycomb patterned polymer composite and its engineering application, *Polym-Plast. Technol.* 57 (2018) 1828–1844, <https://doi.org/10.1080/03602559.2018.1434667>.
- [37] L. Moroni, J.R. de Wijn, C.A. van Blitterswijk, Three-dimensional fiber-deposited PEOT/PBT copolymer scaffolds for tissue engineering: influence of porosity, molecular network mesh size, and swelling in aqueous media on dynamic mechanical properties, *J. Biomed. Mater. Res. A* 75A (2005) 957–965, <https://doi.org/10.1002/jbm.a.30499>.
- [38] Q. Zhao, J. Wang, H. Cui, H. Chen, Y. Wang, X. Du, Programmed shape-morphing scaffolds enabling facile 3D endothelialization, *Adv. Funct. Mater.* 28 (2018), 1801027, <https://doi.org/10.1002/adfm.201801027>.
- [39] E. Fournier, C. Passirani, C.N. Montero-Menei, J.P. Benoit, Biocompatibility of implantable synthetic polymeric drug carriers: focus on brain biocompatibility, *Biomaterials* 24 (2003) 3311–3331, [https://doi.org/10.1016/s0142-9612\(03\)00161-3](https://doi.org/10.1016/s0142-9612(03)00161-3).
- [40] R.J. Bodnar, Anti-angiogenic drugs: involvement in cutaneous side effects and wound-healing complication, *Adv. Wound Care* 3 (2014) 635–646, <https://doi.org/10.1089/wound.2013.0496>.
- [41] Y. Du, B. Lu, J. Chen, J. He, Measurement of the orbital soft tissue volume in Chinese adults based on three-dimensional CT reconstruction, *J. Ophthalmol.* 2019 (2019), 9721085, <https://doi.org/10.1155/2019/9721085>.
- [42] P. Scolozzi, Applications of 3D orbital computer-assisted surgery (CAS), *J. Stomatol.* 118 (2017) 217–223, <https://doi.org/10.1016/j.jormas.2017.05.007>.
- [43] C. Pedemonte, F. Sáez, I. Vargas, L.E. González, M. Canales, K. Salazar, Can customized implants correct enophthalmos and delayed diplopia in post-traumatic orbital deformities? A volumetric analysis, *Int. J. Oral Maxillofac. Surg.* 45 (2016) 1086–1094, <https://doi.org/10.1016/j.ijom.2016.04.007>.
- [44] W.C. Cooper, A method for volume determination of the orbit and its contents by high resolution axial tomography and quantitative digital image analysis, *Trans. Am. Ophthalmol. Soc.* 83 (1985) 546–609.
- [45] B. Unal, A. Kara, S. Aksak, D. Unal, A stereological assessment method for estimating the surface area of cycloids, *Eurasian J. Med.* 42 (2010) 66–73, <https://doi.org/10.5152/eajm.2010.20>.
- [46] N. Acer, B. Sahin, H. Ergür, H. Basaloglu, N.G. Ceri, Stereological estimation of the orbital volume: a criterion standard study, *J. Craniofac. Surg.* 20 (2009) 921, <https://doi.org/10.1097/SCS.0b013e3181a1686d>.